

Article

Cost-Effective and Facile Preparation of Fe₂O₃ Nanoparticles Decorated N-Doped Mesoporous Carbon Materials: Transforming Mulberry Leaf into a Highly Active Electrocatalyst for Oxygen Reduction Reactions

Tingting Zhang ^{1,†}, Lihao Guan ^{1,†}, Changqing Li ¹, Junfeng Zhao ², Manchao Wang ¹, Lin Peng ¹, Jiahui Wang ¹ and Yuqing Lin ^{1,*}

¹ Department of Chemistry, Capital Normal University, Beijing 100048, China; czhangtingting@163.com (T.Z.); guanlihao666@163.com (L.G.); lichangqing19921225@126.com (C.L.); 1150701049@cnu.edu.cn (M.W.); 1150701045@cnu.edu.cn (L.P.); wangjiahui55@126.com (J.W.);

² Zhengzhou Prevention and Treatment Center for Occupational Diseases, Zhengzhou 450003, China; zhjf2010@foxmail.com

* Correspondence: linyuqing@cnu.edu.cn; Tel./Fax: +86-010-6890-3047

† These two authors contributed equally to this work.

Received: 6 January 2018; Accepted: 9 February 2018; Published: 28 February 2018

Abstract: Herein, a promising method to prepare efficient N-doped porous carbon-supported Fe₂O₃ nanoparticles (Fe₂O₃/N-PCs) ORR electrocatalysts is presented. The porous carbon was derived from a biomass i.e., mulberry leaf through a cost-effective approach. The existence of diverse compounds containing carbon, oxygen, nitrogen and sulfur in mulberry leaf benefit the formation and uniform dispersion of Fe₂O₃ nanoparticles (NPs) in the porous carbon. In evaluating the effects of the carbon support on the Fe₂O₃ NPs towards the ORR, we found that the sample of Fe₂O₃/N-PCs-850 (Fe₂O₃/N-PCs obtained at 850 °C) with high surface area of 313.8 m²·g⁻¹ exhibits remarkably superior ORR activity than that of materials acquired under other temperatures. To be specific, the onset potential and reduction peak potential of Fe₂O₃/N-PCs-850 towards ORR are 0.936 V and 0.776 V (vs. RHE), respectively. The calculated number of electron transfer *n* for the ORR is 3.9, demonstrating a near four-electron-transfer process. Furthermore, it demonstrates excellent longtime stability and resistance to methanol deactivation compared with Pt/C catalyst. This study provides a novel design of highly active ORR electrocatalysts from low-cost abundant plant products.

Keywords: oxygen reduction reaction; mulberry leaf; Non-noble metal catalyst; mesoporous carbon material; Fe₂O₃

1. Introduction

The fuel cell with its high-efficiency and low-pollution has been deemed as one of the future power sources; catalysts for cathode reaction referred to as oxygen reduction reaction (ORR) are vital for the scalable commercialization of fuel cell technologies [1–3]. Thus, the ORR as the cornerstone reaction of fuel cells and has drawn an extensive attention, which raises growing interest to explore efficient ORR electrocatalysts. In spite of great achievements made in noble-metal electrocatalysts, the high cost, scarcity and instability impede its further application [4,5]. In this respect, enormous viable noble-metal-free catalysts (Fe, Co, etc.) [6,7], or metal oxide [8], sulphide [9], nitride [10], carbide [11], metal-free carbon based materials [12] and nitrogen-doped carbon [13] have been actively pursued. Among above mentioned catalysts, the application of iron oxide as the electrocatalyst is

rarely reported owing to its dissolution and agglomeration during the operation in fuel cells, which leads to deteriorated electrocatalytic activity towards ORR [14].

To address the problem mentioned above, various catalyst supports with nanostructure have been explored such as carbon materials (porous carbon, active carbon, carbon nanotubes, and graphene) [15–19], carbide [20], mesoporous silica microsphere [21], and conducting substrates [22] to increase the electroactive surface area of catalysts and further enhance their catalytic activity and durability. Recently, Müllen et al. reported a highly efficient cathode catalysts i.e., $\text{Fe}_3\text{O}_4/\text{N-GAs}$, which exhibits remarkable ORR activity [23]. Zhu's group designed a novel 3D heterostructured electrode (SSC-Fe) decorated with amorphous iron oxide ($\text{Fe}_2\text{O}_3/\text{Fe}_3\text{O}_4$), featuring comparable ORR activity to that of a Pt-decorated one [24]. These studies preliminarily indicate that the involvement of Fe_2O_3 may serve as an important factor that boosts ORR for these catalysts. Within the decoration of Fe_2O_3 into the porous carbon, the carbon-based hybrid indicated a remarkably enhanced ORR property. However, the ORR mechanism underpinning Fe_2O_3 has remained incompletely understood thus far due to the complication of decoupling the effect of iron oxide, Fe_3C , Fe_xN , and $\text{N}_x\text{-C}$ in carbon-supported transition-metal nitrogen-doped composites. Furthermore, the electrochemical instability of Fe_2O_3 may result in the transformation to Fe_3O_4 during the synthesis process and severe dissolution in the electrolyte. Fe elements also facilitate the transformation of inactive oxidized N species to the highly active pyridinic-N, pyrrolic-N, and iron-nitrogen bond (Fe-N_x) clusters for $\text{Fe}_2\text{O}_3/\text{N-PCs-850}$, thereby improving the ORR electro-catalytic activity of the as prepared $\text{Fe}_2\text{O}_3/\text{N-PCs-850}$ catalyst [25].

In addition to activity of catalysts, setting up rich porosity of support is also imperative to achieve efficient multidimensional mass and electron transfer pathways of three-phase interface where ORR takes place [26–29]. A typical work was reported to synthesize a kind of carbon nitride electrocatalyst with multiple pore type by incorporating FeCl_3 , XC-72R nanoparticles and $\text{K}_4\text{Fe}(\text{CN})_6$ as iron, carbon and nitrogen source, respectively [30]. Compared with the above approach, biomass such as pomelo peels [11], egg [31], coir [32], and seaweed [33] has attracted increasing popularity into the fabrication of porous carbon support material due to its distinctive good accessibility, environmental friendliness and sustainability. Moreover, it has been proven that the carbon materials obtained from direct thermal pyrolysis of biomass usually catalyse the ORR inefficiently through the two-electron transfer route to form peroxide species, thus, its ongoing oxygen reduction (i.e., four-electron transfer process in ORR) needs further catalysis by the introduction of metallic components [34].

Recently, carbon materials containing heteroatoms have emerged as excellent electrocatalysts for ORR owing to it possessing abundant active sites uniformly distributed throughout the carbon framework with the homogeneous existence of precursor elements in biomass [35–37]. Mulberry leaves are rich in crude protein containing C, O, N, and S [38], which can easily form coordination complexes that act as Fe-N_x active sites, thus making it an ideal source of heteroatoms dopant for the carbon framework that act as catalytic sites with high performance after pyrolysis.

In this work, we propose a cost-effective approach to prepare N-doped porous carbon-supported Fe_2O_3 nanoparticles ($\text{Fe}_2\text{O}_3/\text{N-PCs}$) derived from mulberry leaves as efficient ORR electrocatalysts. The calcination of mulberry leaves and second calcination of carbon matrix after the incorporation of iron can promote the graphitization degree of amorphous carbon to form Fe_2O_3 . Also, during the pyrolysis process, many micropores and microchannels were formed, which contributed to the electron/mass transport and the absorption of oxygen during ORR. Importantly, the confinement of metal oxide NPs within carbon-based substrates can enhance the accessible interface area and to minimize the dissolution and agglomeration of NPs, thus contributing to the enhancement of the electrochemical activity and stability of the $\text{Fe}_2\text{O}_3/\text{N-PCs}$ hybrids. Moreover, the employment of porous carbon support can realize the high specific surface area and multi-scale porous structure in as prepared catalysts for more efficient mass transfer and dynamic reactions. The above unique properties will considerably enhance the ORR performances in electrochemical systems. Therefore, it is expected that our work may provide a rational design for the synthesis of heteroatom-doped porous carbon supported metal oxide catalysts on a large scale.

2. Results and Discussion

The $\text{Fe}_2\text{O}_3/\text{N-PCs}$ composites were prepared by using a hydrothermal, heat treatment processes together with a freeze-drying method (Scheme 1), in which organic-rich biomass, i.e., mulberry leaves, serve as a carbon and nitrogen source; FeCl_3 acted as an iron source and contributed to the formation of Fe_2O_3 during the calcination. The porous structures of $\text{Fe}_2\text{O}_3/\text{N-PCs}$ and N-PC were collected by SEM images. As shown in Figure 1A,B, the typical $\text{Fe}_2\text{O}_3/\text{N-PCs}$ exhibits a mesoporous structure with the pore sizes around 100 nm. The N-PCs exhibits an amorphous porous structure which is shown in Figure 1C,D. According to the SEM images of $\text{Fe}_2\text{O}_3/\text{N-PCs}$ and N-PCs, the formation of Fe_2O_3 with a structure of mesoporous can be observed. The formation of mesopores in $\text{Fe}_2\text{O}_3/\text{N-PCs}$ and N-PCs is associated with the decomposition of diverse organic compounds that exist in mulberry leaves with the release of pyrolysis gases. Also, we can speculate that such a porous structure can promote the accumulation of abundant iron oxide during the heat treatment process so as to facilitate the mass transfer and obtain more active sites. It was reported that the amorphous iron oxide can facilitate mass transfer, which can reduce the area specific resistance of the 3D heterostructured cathode to 50% of that of the unmodified one by $0.01 \Omega \text{ cm}^2$ only [23]. Meanwhile, the C, N, Fe and O element ratios in $\text{Fe}_2\text{O}_3/\text{N-PCs-800}$, $\text{Fe}_2\text{O}_3/\text{N-PCs-850}$, and $\text{Fe}_2\text{O}_3/\text{N-PCs-900}$ from EDX analysis are listed in Table S1.

N_2 adsorption and desorption isotherm was performed to investigate the porosity of $\text{Fe}_2\text{O}_3/\text{N-PCs}$ (Figure 2A). The specific surface area of $\text{Fe}_2\text{O}_3/\text{N-PCs-800}$, 850, 900 were measured to be $188.6 \text{ m}^2 \cdot \text{g}^{-1}$, $313.8 \text{ m}^2 \cdot \text{g}^{-1}$ and $139.5 \text{ m}^2 \cdot \text{g}^{-1}$ respectively, in which $\text{Fe}_2\text{O}_3/\text{N-PCs-850}$ has the highest surface area. Moreover, Figure 2B reveals a typical type IV pattern with an H4 hysteresis loop, demonstrating the existence of a developed mesoporous structure in $\text{Fe}_2\text{O}_3/\text{N-PCs-850}$ with a narrower pore size distribution of about 3.5 nm. Thus, $\text{Fe}_2\text{O}_3/\text{N-PCs-850}$ with the highest surface area may contribute to the exposure of catalytic active sites and mass transport involved in ORR, which is favorable for improved electrocatalytic performance.



Scheme 1. The schematic illustration of the preparation process for $\text{Fe}_2\text{O}_3/\text{N-PCs-850}$ nanoporous structures material.

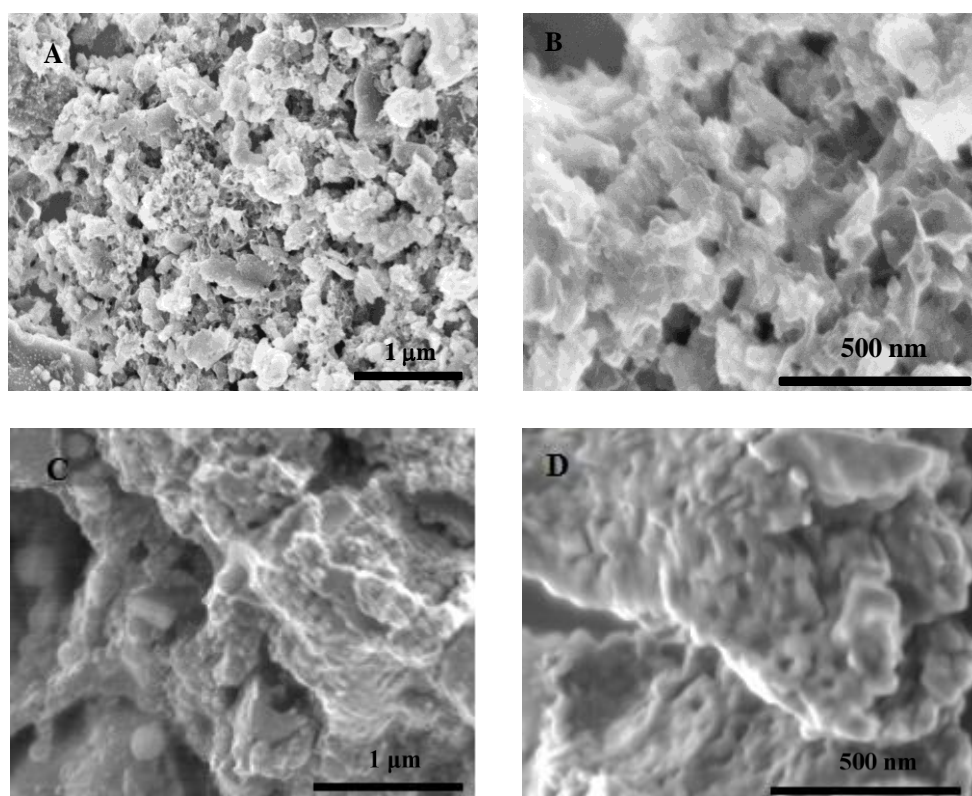


Figure 1. Scanning electron microscopy images of $\text{Fe}_2\text{O}_3/\text{N-PCs-850}$ (A,B) and bare N-doped porous carbon support alone without Fe_2O_3 (C,D).

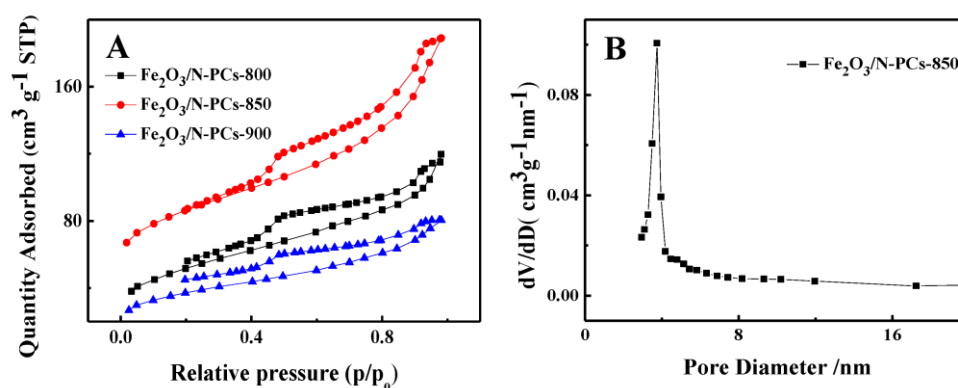


Figure 2. Nitrogen desorption-adsorption isotherm of $\text{Fe}_2\text{O}_3/\text{N-PCs-800}$, $\text{Fe}_2\text{O}_3/\text{N-PCs-850}$, $\text{Fe}_2\text{O}_3/\text{N-PCs-900}$.

It has been reported that mesoporous structures can improve the mass transport and diffusion of oxygen molecules where the ORR process takes place owing to the presence of abundant active sites for ORR in a kinetically controlled region [39–41]. Therefore, it is speculated that $\text{Fe}_2\text{O}_3/\text{N-PCs-850}$ with highest surface area can contribute to the exposure of catalytic sites and enhance the ORR-related electro/mass transfer favoring the improved electrocatalytic performance in the next investigation.

XRD patterns of the $\text{Fe}_2\text{O}_3/\text{N-PCs}$ composites at different pyrolysis temperatures are illustrated in Figure 3A. As shown, all pyrolyzed samples show (002) inter plane with diffraction peaks located at around 26.381° , corresponding to the graphitic carbon phase (PDF#41-1487). From Figure 3A, it can be deduced that diverse phases of Fe_2O_3 were produced at a certain temperature. Compared with all phases of powder diffraction files (PDF) of Fe_2O_3 (Figure S1), three clearly observed diffraction

peaks at 32.802° , 29.950° , 22.150° corresponding to the crystal plane $(\bar{4}20)$ $(\bar{4}11)$ (220) , respectively, match well with Fe_2O_3 (PDF#40-1139) in all $\text{Fe}_2\text{O}_3/\text{N-PCs}$ composites, and diffraction peaks at 31.130° , 33.816° corresponding to the crystal plane (113) (116) , respectively, match well with Fe_2O_3 (PDF#16-0653) demonstrating efficient assembly between the Fe_2O_3 NPs and the carbon support. Fe_2O_3 (PDF#40-1139) was defined as $\gamma\text{-Fe}_2\text{O}_3$ and Fe_2O_3 (PDF#16-0653) was defined as $\varepsilon\text{-Fe}_2\text{O}_3$, respectively. Also, the proportions of different phases of Fe_2O_3 are not the same at different temperatures. With the increase of temperature, the content of $\varepsilon\text{-Fe}_2\text{O}_3$ also increased. It is believed the formation of Fe_2O_3 NPs originate from the combination of Fe^{3+} and the oxygen principally created from the O-containing functional groups at the surface of the N-doped carbon material during the pyrolysis process at high temperature, which leads the doping-induced charge and/or spin redistribution in the carbon framework, thus contributing to the enhanced activity of the as prepared catalyst.

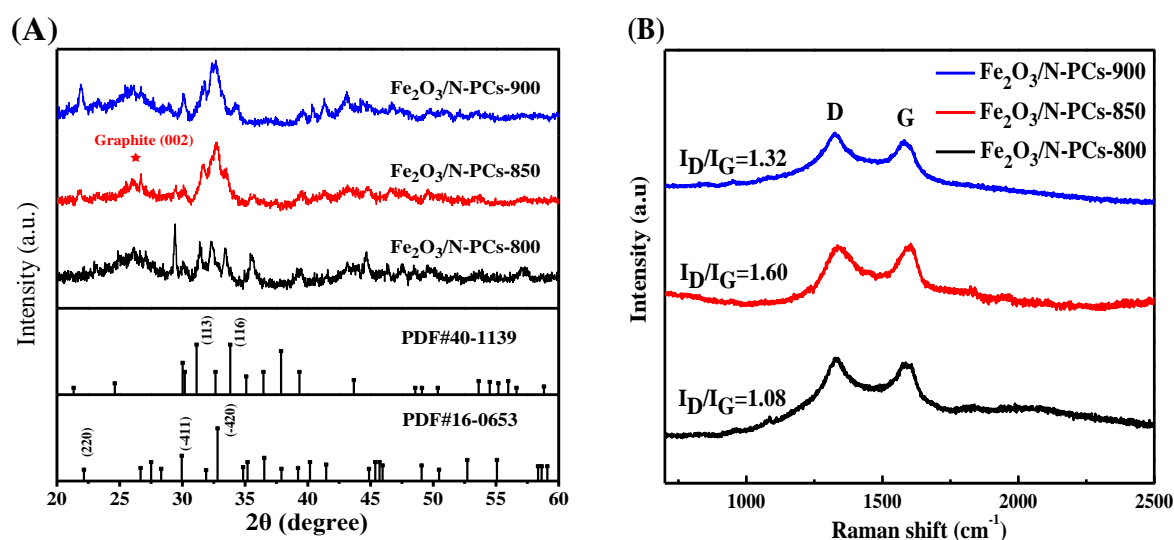


Figure 3. XRD pattern (A) and Raman spectra (B) of $\text{Fe}_2\text{O}_3/\text{N-PCs-800}$, $\text{Fe}_2\text{O}_3/\text{N-PCs-850}$ and $\text{Fe}_2\text{O}_3/\text{N-PCs-900}$.

Raman analysis was performed to figure out the graphitization degree of the obtained carbon materials. As can be seen in Figure 3B, the two typical peaks around 1360 and 1580 cm^{-1} refer to the D band and G band of $\text{Fe}_2\text{O}_3/\text{N-PCs}$ materials, respectively. It was reported that the peak from 1360 cm^{-1} was attributed to sp^3 carbon atoms at the defects and disorder in the carbon material [42]. The D band is associated with the sp^3 carbons at defective sites. The G band corresponds to Raman scattering of phonons in the vicinity of the Gamma point and is related to the E_{2g} stretching vibration mode of sp^2 carbon atoms. According to previous research, the relative intensity ratio of I_D/I_G is assigned to the number of defect sites [43]. As Figure 3B shows, the D and G bands are existent in all of the prepared catalysts, the I_D/I_G ratio was calculated to be 1.08 for $\text{Fe}_2\text{O}_3/\text{N-PCs-800}$, 1.60 for $\text{Fe}_2\text{O}_3/\text{N-PCs-850}$, and 1.32 for $\text{Fe}_2\text{O}_3/\text{N-PCs-900}$. Such enormous defects are associated with the incorporation of heteroatoms into the sp^2 -carbon structure, which are anticipated to result in the boosting of ORR activity [43,44].

XPS data indicates the surface properties of the $\text{Fe}_2\text{O}_3/\text{N-PCs}$ electrocatalysts. The XPS spectrum (Figure 4A) declares the existence of C, O, N, and Fe on the obtained catalysts. However, in all these three catalysts, the Fe 2p peak has a weakest signal owing to its trace amount. Figure 4B shows high-resolution C 1s spectra for $\text{Fe}_2\text{O}_3/\text{N-PCs-850}$. The overlapped high-resolution C 1s peak decomposed into three components, corresponding to the C-C (284.4 eV), C-O and C=N (285.9 eV), and C-O-C and C-N (288.5 eV) [41]. Figure 4C shows that the Fe 2p spectrum could be deconvoluted into two peaks at around 711.4 and 724.8 eV , which could be ascribed to the binding energies of the $2p_{3/2}$ and $2p_{1/2}$ bands of Fe^{3+} associated with the Fe-N_x moieties, respectively [29,45]. The other two samples' high-resolution Fe 2p XPS spectrum was plotted in Figure S2. These results together with the

electron microscopy analysis validated the formation of Fe₂O₃ nanoparticles anchored on N-doped carbon nanostructures.

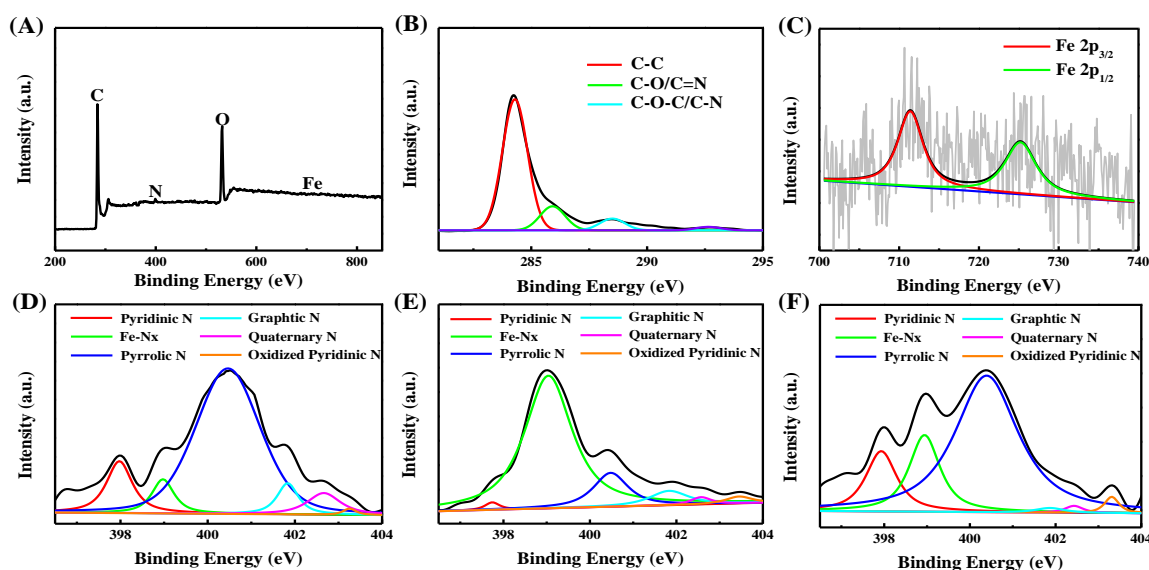


Figure 4. (A) XPS survey spectra of Fe₂O₃/N-PCs-850; High-resolution C 1s (B) and Fe 2p (C) XPS spectrum of Fe₂O₃/N-PCs-850; High-resolution N 1s XPS spectrum of Fe₂O₃/N-PCs-800 (D), Fe₂O₃/N-PCs-850 (E) and Fe₂O₃/N-PCs-900 (F).

Recently, it has been reported that ORR activity has close connection to N content; thus, nitrogen species in Fe₂O₃/N-PCs were carefully analyzed [46]. The N1s XPS spectra of all samples were deconvoluted into six peaks (Figure 4D–F), namely pyridinic N (397.9 ± 0.2 eV), Fe-Nx (399.0 ± 0.1 eV), pyrrolic N (400.4 ± 0.1 eV), graphitic N (401.8 ± 0.3 eV), quaternary N (402.6 ± 0.2 eV), and oxidized pyridinic N (403.3 ± 0.2 eV) [47,48]. The percentage of each N bonding of three samples was also described in Figure 5. The atom contents of the Fe coordinated nitrogen of Fe₂O₃/N-PCs-850 is 74.61% (calculated from the peak area of the iron-associated pyridinic N), which is higher than Fe₂O₃/N-PCs-800 and Fe₂O₃/N-PCs-900. The pyrrolic N peaks were smaller at Fe₂O₃/N-PCs-850 but got bigger again at higher temperature treatment (Fe₂O₃/N-PCs-900). It was suspected that Fe-Nx may decompose to from pyrrolic N at higher temperatures. Additionally, characterization of XPS of bare N-PCs without Fe was also performed (Figure S3), indicating there was no Fe-Nx moieties and Fe content in the sample. These results correlate to Fe₂O₃/N-PCs-850 having the best ORR activity, since it may induce the affluent formation of Fe₂O₃ and Fe-Nx, which can serve as electrocatalytic active sites for ORR. As reported in previous studies, pyridinic-N can be coordinated with transition metal elements, enabling the formation of Fe-Nx moieties onto the Fe₂O₃/N-PCs-850, which should act as active sites for the ORR [49]. In combination with the XRD results and N 1s XPS spectra discussed above, it can be concluded that Fe may bind to pyridinic N to form Fe-Nx species and the optimum temperature for the formation of this structure is 850 °C. The abundant porous structures, vast nitrogen atoms, and large amounts of Fe-Nx existing in the Fe₂O₃/N-PCs-850 sample play the most important roles in promoting its ORR activity, ensuring that the Fe₂O₃/N-PCs-850 sample has promising ORR catalytic activity [25]. Meanwhile, some literature studies proved that pyridinic-N and pyrrolic-N also make a contribution to the ORR electro-catalytic activity [49]. Quaternary N in the pyrolyzed composites are conducive to catalyze the ORR and can serve as catalytically active sites for oxygen reduction [47]. The lone-pair electrons of pyridinic N and pyrrolic N can act as metal coordination sites; the sum of quantities of the three kinds of active nitrogens are in high proportion in Fe₂O₃/N-PCs-850 suggesting its high performance towards ORR [50]. Oxidized pyridinic Ns

do not significantly contribute to the ORR performance and are unstable under fuel cell operating conditions [51].

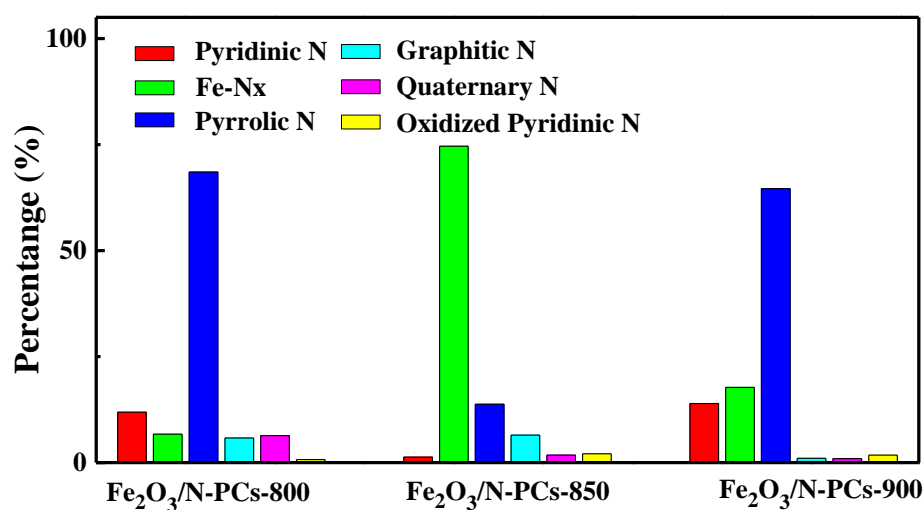


Figure 5. The percentage of six nitrogen species in Fe₂O₃/N-PCs at different temperature.

To investigate the ORR activities of Fe₂O₃/N-PCs-800, Fe₂O₃/N-PCs-850, and Fe₂O₃/N-PCs-900 for ORR, CV measurements were performed in N₂ or O₂-saturated 0.1 M KOH. As displayed in Figure 6, a well-defined ORR reduction peak emerged at 0.776 V and the onset potential of the catalyst for ORR is 0.936 V in the CV measurements, which is comparable to the value of 0.946 V vs. RHE of the Pt/C ref. [10], demonstrating the predominant ORR electrocatalytic activity of Fe₂O₃/N-PCs-850. Moreover, Fe₂O₃/N-PCs-800 and Fe₂O₃/N-PCs-900 catalyst show that the ORR peak potential occurs at 0.756 V and 0.696 V and the onset potentials for ORR are 0.916 V and 0.85 V, respectively. These results validated the superior electrocatalytic activity of Fe₂O₃/N-PCs-850. On the other hand, the ORR activity of Fe₂O₃/N-PCs-850 is much better than that of N-PCs-850 (Figure S4) with the reduction peak potential of about 110 mV positive than the N-PCs-850 catalyst, the improved intrinsic ORR activity of the Fe₂O₃/N-PCs-850 catalyst can be assigned to a large amount of Fe-N_x active sites between the Fe₂O₃ nanoparticles and the N-doping in the mesoporous carbon structure. Importantly, a moderate pyrolysis temperature was quite significant to prepare superior ORR catalytic performance, which may be ascribed to such temperatures and is beneficial to form more catalytic active sites. The surface area/pore volume ratio and graphitization degree also are key factors that affect the exposure of catalytic active sites and mass transport rate. However, a much higher pyrolysis temperature (e.g., 1000 °C) will lead to the increase of the quantity of disordered carbon in the graphite carbon, which would lower the electron transfer rate and thus results in inferior ORR performance [29].

To understand the detailed mechanism of the ORR on such catalysts is quite important. ORR through the adsorbed HO₂[−] intermediate will be analyzed by the RRDE and RDE voltammograms. The RRDE measurement was applied to quantitatively determine the HO₂[−] generation rate; the percentage of HO₂[−] were obtained by the followed equations:

$$\text{HO}_2\% = 200 (I_r/N)/(I_d + I_r/N)$$

where I_d and I_r corresponds the disk current and ring current, respectively. N refers as the current collection efficiency of the Pt ring, which was calculated to be 0.4 [52]. From Figure 6B, the HO₂[−] yield value for the Fe₂O₃/N-PCs-850 during the ORR process is 5% at the potentials of 0.166 V.

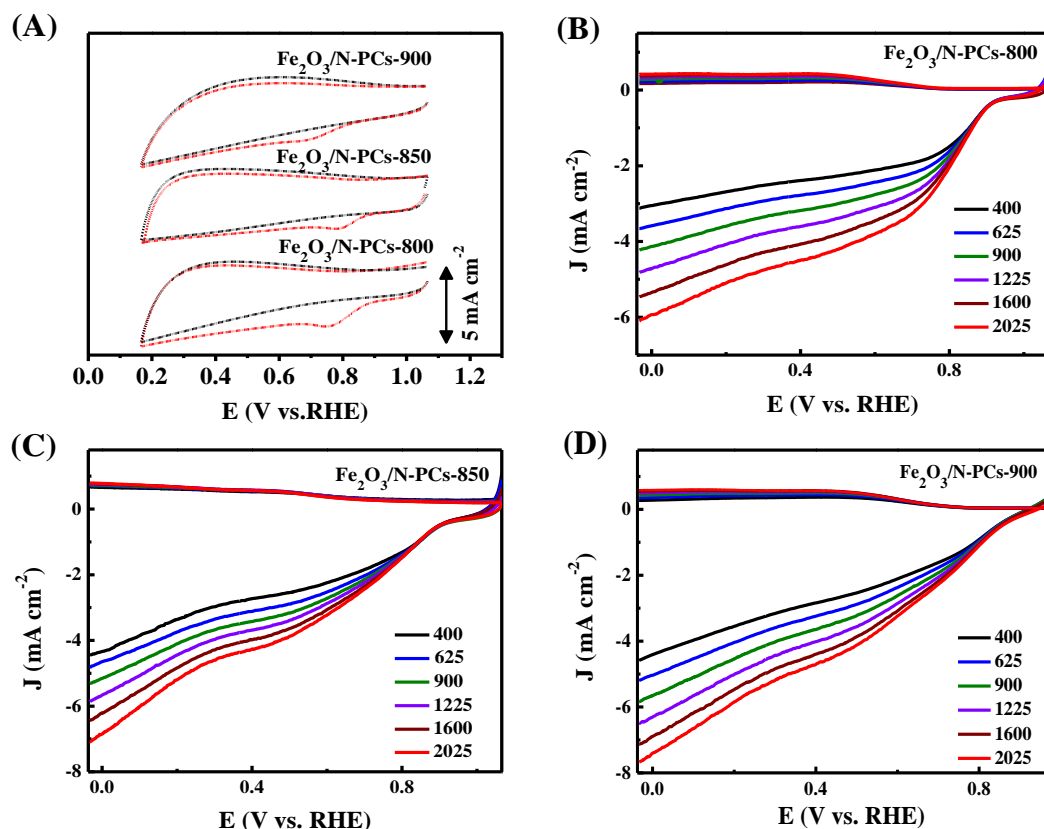


Figure 6. Cyclic voltammograms of $\text{Fe}_2\text{O}_3/\text{N-PCs-800}$, $\text{Fe}_2\text{O}_3/\text{N-PCs-850}$ and $\text{Fe}_2\text{O}_3/\text{N-PCs-900}$ (A) modified GC electrodes in O_2 - and N_2 -saturated 0.1 M KOH at a scan rate of $10 \text{ mV}\cdot\text{s}^{-1}$. LSV curves of $\text{Fe}_2\text{O}_3/\text{N-PCs-800}$ (B), $\text{Fe}_2\text{O}_3/\text{N-PCs-850}$ (C) and $\text{Fe}_2\text{O}_3/\text{N-PCs-900}$ (D) on RRDE at a scan rate of $5 \text{ mV}\cdot\text{s}^{-1}$ with various rotation rates.

To deeply understand the route and kinetic process of the ORR, LSV measurement of the $\text{Fe}_2\text{O}_3/\text{N-PCs-850}$ catalyst were conducted by RRDE technique with rotation speed ranging from 400–2025 rpm in O_2 -saturated 0.1 M KOH (Figure 6C). These curves (Figure 6B–D) demonstrate an increasing current density with the ascending rotation rates owing to the accelerated diffusion of electrolyte. The LSV curve of $\text{Fe}_2\text{O}_3/\text{N-PCs-800}$, $\text{Fe}_2\text{O}_3/\text{N-PCs-850}$ and $\text{Fe}_2\text{O}_3/\text{N-PCs-900}$ in 1600 rpm derived from the RRDE measurements were compared in Figure S5A, and LSV curves of 20% Pt/C and $\text{Fe}_2\text{O}_3/\text{N-PCs-850}$ were also compared in Figure S5B. As expected, the K-L plots for $\text{Fe}_2\text{O}_3/\text{N-PCs-850}$ showed good linear functions between j^{-1} and $\omega^{-1/2}$ (Figure 7B). The electron transfer number (n) for ORR can be obtained from the Koutecky–Levich equation:

$$1/J = 1/J_K + 1/J_L = 1/J_K + 1/(B\omega^{-1/2})$$

$$B = 0.2 nFv^{-1/6}D_{\text{O}_2}^{2/3}C_{\text{O}_2}$$

where J_K is the kinetic current density of the ORR, ω is rotation speed, n is the electron transfer number per oxygen molecule, F is the Faraday constant ($96485 \text{ C}\cdot\text{mol}^{-1}$), v is the kinematic viscosity of KOH ($0.01 \text{ cm}^2\cdot\text{s}^{-1}$), D_{O_2} corresponds to the diffusion coefficient of O_2 ($1.9 \times 10^{-5} \text{ cm}^2\cdot\text{s}^{-1}$) and C_{O_2} is the concentration of O_2 in the solution ($1.13 \times 10^{-6} \text{ mol}\cdot\text{cm}^{-3}$).

It has been widely acknowledged that the direct four electrons are more favorable for the ORR process, thus, the transferred electron numbers (n) were calculated in Figure 7 by the RDE measurements. The $\text{Fe}_2\text{O}_3/\text{N-PCs-850}$ has the transferred electron numbers (n) of 3.9, involving a four-electron ORR process, while the transferred electron numbers for $\text{Fe}_2\text{O}_3/\text{N-PCs-800}$ and $\text{Fe}_2\text{O}_3/\text{N-PCs-900}$ were only 3.6 and 3.5, respectively. The high selectivity for the four-electron transfer

pathway of Fe₂O₃/N-PCs-850 can be associated with the Fe-N_x active sites created by doped N and Fe₂O₃ nanoparticles. In addition, compared with the reported electrocatalysts derived from biomass materials, as shown in Table 1, the onset potential together with electron transfer number of the optimal Fe₂O₃/N-PCs-850 catalyst are comparable to other excellent catalysts. Based on the above results, we believe that the superior ORR activity of Fe₂O₃/N-PCs-850 could be assigned to synergistic effects of the enriched graphitic N-doped carbons and Fe₂O₃ nanoparticles together with the high surface area of Fe₂O₃/N-PCs-850.

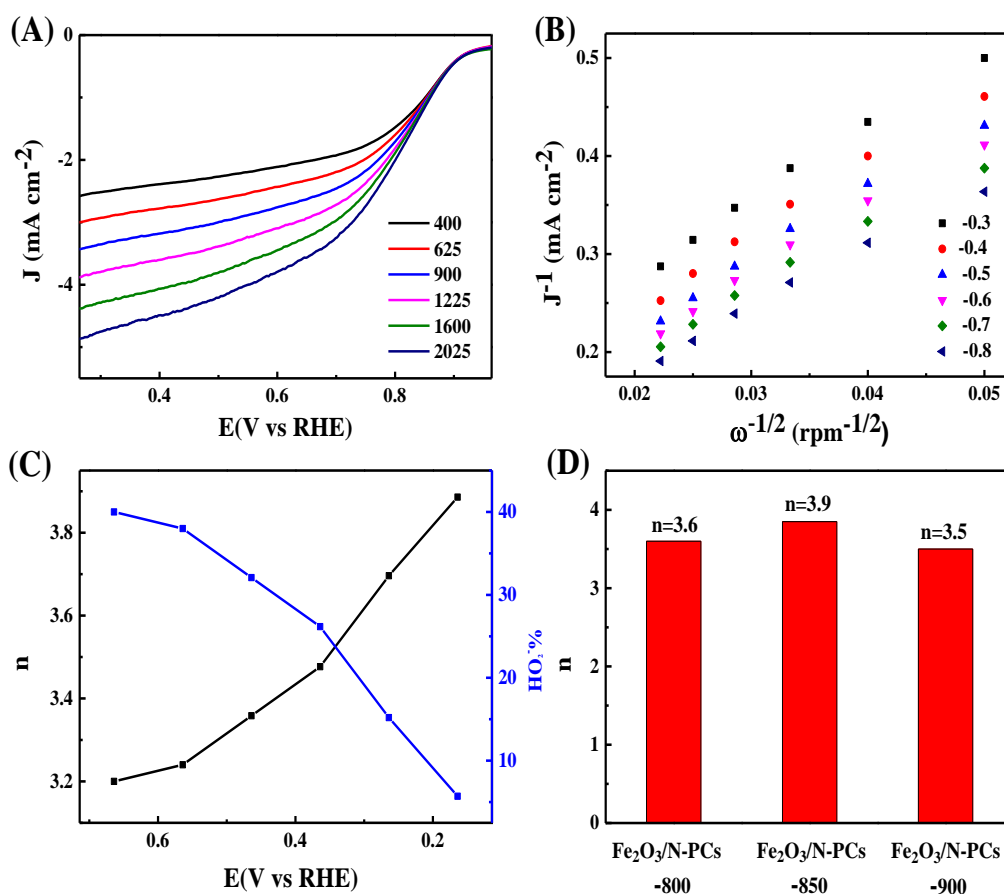


Figure 7. The data derived from the RDE measurements. (A) The LSV curves of ORR for Fe₂O₃/N-PCs-850/GC at different rotation speeds; (B) K-L plots at different potentials of Fe₂O₃/N-PCs-850 in 0.1 M KOH at a scan rate of 5 mV·s⁻¹; (C) HO₂⁻ yields and the electron transfer number during the ORR process of Fe₂O₃/N-PCs-850/GC; (D) The transferred electron numbers of the designed catalysts calculated from RDE.

Table 1. ORR catalytic performances comparison of electrocatalysts derived from biomass materials.

Catalyst	Onset Potential (V)	Electron Transfer Number (n)	Electrolyte	Type of Biomass	Reference
Fe/Fe ₂ O ₃ @Fe-N-C-1000	0.92	4.00	0.1M KOH	Shrimp Shells	[29]
Egg-CMS	0.84	3.11	0.1M KOH	Eggs	[31]
HDPC-800	0.95	3.99	0.1M KOH	Tea Leaves	[46]
N-P-Fe-C	0.957	3.99	0.1M KOH	Corn Silk	[53]
LY-1000	0.913	3.78	0.1M KOH	Ginkgo Leaves	[54]
Fe/N/CNT@PCF	0.862	3.90	0.1M KOH	Catkins	[25]
HAZ-800	0.87	3.60	0.1M KOH	Bamboo Fungus	[55]
N-C@CNT-900	0.94	3.90	0.1M KOH	Enoki Mushroom	[56]
Fe ₂ O ₃ /N-PCs-850	0.93	3.90	0.1M KOH	Mulberry leaves	This work

To examine the possible crossover effects, the electrocatalytic durability of $\text{Fe}_2\text{O}_3/\text{N-PCs-850}$ and 20% Pt/C against the poisoning of methanol were measured by injecting 3 mL methanol at 350 s in an O_2 -saturated alkaline solution. Figure 8A shows that the ORR current density of commercial Pt/C catalyst had a sudden change upon the introduction of methanol owing to the electrochemical oxidation of methanol. However, the $\text{Fe}_2\text{O}_3/\text{N-PCs-850}$ retained more than 75% of its initial current density under the same condition, revealing its superior selectivity over 20% Pt/C catalyst, which remained about 40%. This may be explained by the excellent stability of the synergistic effect of N and Fe as the active sites for oxygen reduction reaction among the carbon framework. The stability of the prepared $\text{Fe}_2\text{O}_3/\text{N-PCs-850}$ was also examined by current-time chronoamperometric measurement at -0.2 V for 3000 s in 0.1 M KOH solution with O_2 -saturated. After testing for 3000 s, slight performance attenuation (23.2%) was observed for $\text{Fe}_2\text{O}_3/\text{N-PCs-850}$ in Figure 8B, whereas performance degradation of 20% Pt/C catalyst degraded significantly with an obvious current loss of 67.2%. These results again demonstrate the advantage of the $\text{Fe}_2\text{O}_3/\text{N-PCs-850}$ over 20% Pt/C catalyst.

Thus, from the above experimental data and analysis results, the following factors can explain the reason that our $\text{Fe}_2\text{O}_3/\text{N-PCs-850}$ catalyst presents the best ORR catalytic activity. On the one hand, pyrolyzed biomass mulberry leaf with excellent porous structures has a large surface area that could carry more exposed active sites. On the other hand, the maximum Fe-N_x clusters, pyridinic-N, and pyrrolic-N dispersed on the Fe/N/CNT@PCF act as catalytic active sites for catalyzing the ORR. Consequently, the $\text{Fe}_2\text{O}_3/\text{N-PCs-850}$ catalyst displays the best ORR catalytic activity compared to the commercial Pt/C with superior methanol tolerance ability and durability.

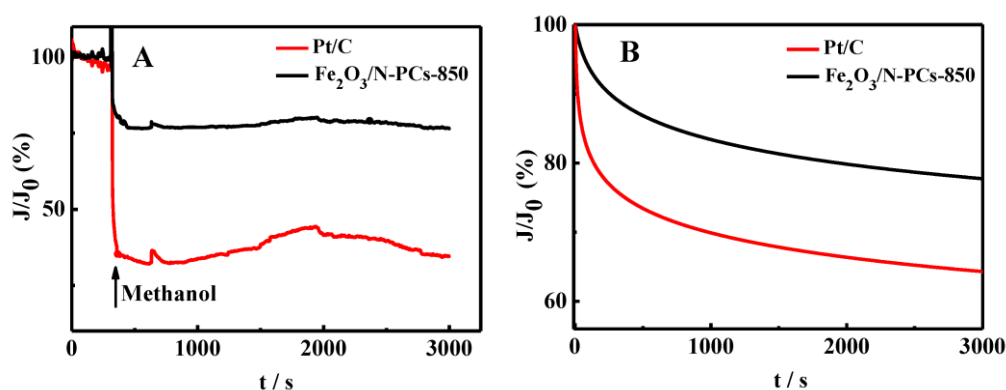


Figure 8. (A) I-t responses at the Pt/C (20%) and $\text{Fe}_2\text{O}_3/\text{N-PCs-850}$ at -0.2 V in O_2 -saturated 0.1 M KOH. The arrow refers to the introduction of 3.0 M methanol; (B) I-t responses of $\text{Fe}_2\text{O}_3/\text{N-PCs-850}$ and 20% Pt/C at -0.3 V in the O_2 -saturated 0.1 M KOH.

3. Experimental

3.1. Chemicals

FeCl_3 , KOH, 5 wt % Nafion perfluorinated resin solution and 20 wt % commercial Pt/C were obtained from Sigma-Aldrich (St. Louis, MO, USA). A Milli-Q plus water purification system (18 M Ω , Milli-pore Co., Ltd., Billerica, MA, USA) was used to obtain ultra-pure water and used in all parts that related to aqueous environments.

3.2. Apparatus

SEM images were collected on a Hitachi S-2600 N scanning electron microscope (Tokyo, Japan). EDX data were obtained through Flash EA 1112 (Waltham, MA, USA). XPS spectra were recorded on a VG Micro-tech ESCA 2000 equipment (Nanjing, Jiangsu, China). RRDE electrodes (RRDE-3A, BAS, Tokyo, Japan) with a Pt ring and glass carbon electrode were used. The collection efficiency of the RRDE was calculated to be 0.4 using the $\text{Fe}(\text{CN})_6^{3-/4-}$ redox couple. Electrochemical measurements

were conducted in CHI600E electrochemical workstation with glassy carbon electrode (3 mm in diameter), a platinum wire and a Ag/AgCl (with KCl saturated) electrode forming the three-electrode cell system

3.3. Preparation of Fe₂O₃/N-PCs Catalysts

First, 10.0 g clean mulberry leaves was dried in the air and smashed into powder. Subsequently, the mulberry powder was transferred into a 100 mL autoclave with 60 mL distilled water added. Then, putting the autoclave into an oven, heated at the temperature of 180 for 10 h and the brown carbonaceous product was obtained after freeze drying for 12 h. The obtained product was put into a quartz tube reactor and transferred into a tube furnace and pyrolyzed in N₂ atmosphere at 850 °C for two hours at 4 °C min⁻¹ heating rate. Then, the N-doped carbon material was prepared. After that, 150.0 mg of the above N-doped carbon material was dispersed into 10 mL distilled water, adding 3.0 mg of FeCl₃ into the above mixture solution and stirred with magnet. The dried mixture was obtained through a freeze drying method for 12 h. The final dried mixture annealed in a flow of N₂ atmosphere at 850 C for 2 h with the heating rate of 4 °C · min⁻¹ to obtain the typical Fe₂O₃/N-PCs-850. For comparison, we also prepared Fe₂O₃/N-PCs catalysts at 800 and 900 °C which were denoted as Fe₂O₃/N-PCs-800 and Fe₂O₃/N-PCs-900, respectively. The contrast materials without Fe prepared under temperatures of 800, 850, 900 were also synthesized by the same steps as Fe₂O₃/N-PCs just escaping the addition of FeCl₃ aqueous solution, which were defined as N-PCs-800, N-PCs-850, N-PCs-900, respectively.

3.4. Electrochemical Measurements

The RRDE electrode with a rotating glassy carbon (GC) disk electrode (4 mm diameter) and a platinum ring electrode (ALS RRDE-2, Tokyo, Japan), and a GC electrode were used as working electrode in this study. The preparation of working electrode was as follows: the glassy carbon (GC) working electrode was treated with 1.0 and 0.05 μm alumina slurry prior to each use, then sonicating it with deionized water and ethanol; 6 mg Fe₂O₃/N-PCs catalyst was ultrasonically dispersed in ethanol (1 mL) to obtain 6 mg·mL⁻¹ catalytic ink. After that, 5 μL of the dispersion was dropped onto a GC electrode using a micropipett, covering 2.5 μL nafion solution (0.05 wt % in ethanol) subsequently. Linear sweep voltammetry (LSV) was recorded from 0.2 to -1.0 V, the Fe₂O₃/N-PCs catalyst modified GC was scanned at a scan rate of 10 mV·s⁻¹ to evaluate the ORR activity of catalysts in 0.1 M KOH with O₂-saturated. To acquire quantitative data of the ORR activity, LSV experiment was applied on the catalyst-coated RRDE at a scan rate of 5 mV·s⁻¹ KOH solution with O₂-saturated at different rotation rates ranging from 400 to 2025 r·min⁻¹. In analyzing ORR performance, the working potentials versus Ag/AgCl were converted to a reversible hydrogen electrode (RHE).

4. Conclusions

Fe₂O₃/N-PCs electrocatalyst leaves were prepared using a cost-effective, easy process from the highly accessible plant biomass mulberry. The catalyst exhibited highly remarkable ORR activity, excellent stability and tolerance to methanol deactivation effects compared with commercial 20% Pt/C catalyst. The superior activities were ascribed to a large amount of Fe-N_x active sites between the Fe₂O₃ nanoparticles decoration and the N doping in the carbon nanostructure, as well as the mesoporous structure with large surface area creating more catalytic active sites. This work provided a rational design for large-scale production of highly effective electrocatalysts in a cost-effective way from the abundant recyclable mulberry leaves without using any activation and templating agents.

Supplementary Materials: The following are available online at www.mdpi.com/2073-4344/8/3/101/s1, Figure S1: All the Powder Diffraction Files (PDF) of Fe₂O₃ from Joint Committee on Powder Diffraction Standards, PDF#16-0653 (A) PDF#21-0920, (B) PDF#40-1139 (C) PDF#33-0664 (D) PDF#39-0238 (E), PDF#47-1409 (F), Figure S2: The high-resolution Fe 2p XPS spectra of Fe₂O₃/N-PCs-800(A) and Fe₂O₃/N-PCs-900(B), Figure S3: (A) N1s XPS spectra for the N-PCs-850 without Fe, (B) The percentage of five kinds of N species in N-PCs-850 without Fe. Figure

S4: (A) Cyclic voltammograms of Fe₂O₃/N-PCs samples modified GC electrodes in an O₂-saturated 0.1 M KOH at a scan rate of 10 mV s⁻¹ and LSVs of N-PCs-800 (B), N-PCs-850 (C), N-PCs-900 (D) on RRDE in 0.1 M KOH with various rotation rates at a scan rate of 5 mV s⁻¹, Figure S5: (A) The LSV curves of the three kinds of designed catalysts at 1600 rpm derived from the RRDE measurements. (B) Both 20% Pt/C and Fe₂O₃/N-PCs-850 LSV curves derived from the RDE measurements at 1600 rpm, Table S1: C, N, Fe and O element ratios in Fe₂O₃/N-PCs-800, Fe₂O₃/N-PCs-850, and Fe₂O₃/N-PCs-900 from EDX analysis.

Acknowledgments: This work was financially supported by National Natural Science Foundation (21575090), Beijing Municipal Natural Science Foundation (2162009), Youth Talent Project of the Beijing Municipal Commission of Education (CIT&TCD201504072), Youth Innovative Research Team of Capital Normal University and the Project of Construction of Scientific Research Base by the Beijing Municipal Education Commission.

Author Contributions: Tingting Zhang and Yuqing Lin conceived and designed the experiments; Tingting Zhang, Lihao Guan, Manchao Wang, Lin Peng, and Jiahui Wang performed the experiments; Lihao Guan and Changqing Li analyzed the data; Yuqing Lin and Junfeng Zhao contributed reagents/materials/analysis tools; Lihao Guan, Tingting Zhang and Yuqing Lin wrote the paper.

Conflicts of Interest: The authors declare no conflict of interest.

References

1. Bashyam, R.; Zelenay, P. A Class of Non-Precious Metal Composite Catalysts for Fuel Cells. *Nature* **2006**, *443*, 63–66. [[CrossRef](#)] [[PubMed](#)]
2. Dai, L.; Xue, Y.; Qu, L.; Choi, H.-J.; Baek, J.-B. Metal-Free Catalysts for Oxygen Reduction Reaction. *Chem. Rev.* **2015**, *115*, 4823–4892. [[CrossRef](#)] [[PubMed](#)]
3. Qiao, X.; Liao, S.; You, C.; Chen, R. Phosphorus and Nitrogen Dual Doped and Simultaneously Reduced Graphene Oxide with High Surface Area as Efficient Metal-Free Electrocatalyst for Oxygen Reduction. *Catalysts* **2015**, *5*, 981–991. [[CrossRef](#)]
4. Zhou, X.; Qiao, J.; Yang, L.; Zhang, J. A Review of Graphene-Based Nanostructural Materials for Both Catalyst Supports and Metal-Free Catalysts in Pem Fuel Cell Oxygen Reduction Reactions. *Adv. Energy Mater.* **2014**, *4*, 1289–1295. [[CrossRef](#)]
5. Osmieri, L.; Escudero-Cid, R.; Armandi, M.; Videla, A.H.M.; Fierro, J.L.G.; Ocón, P.; Specchia, S. Fe-N/C Catalysts for Oxygen Reduction Reaction Supported on Different Carbonaceous Materials. Performance in Acidic and Alkaline Direct Alcohol Fuel Cells. *Appl. Catal. B* **2017**, *205*, 637–653. [[CrossRef](#)]
6. He, C.; Zhang, T.; Sun, F.; Li, C.; Lin, Y. Fe/N Co-Doped Mesoporous Carbon Nanomaterial as an Efficient Electrocatalyst for Oxygen Reduction Reaction. *Electrochim. Acta.* **2017**, *231*, 549–556. [[CrossRef](#)]
7. Wei, Q.; Tong, X.; Zhang, G.; Qiao, J.; Gong, Q.; Sun, S. Nitrogen-Doped Carbon Nanotube and Graphene Materials for Oxygen Reduction Reactions. *Catalysts* **2015**, *5*, 1574–1602. [[CrossRef](#)]
8. Zhang, T.; He, C.; Sun, F.; Ding, Y.; Wang, M.; Peng, L.; Wang, J.; Lin, Y. Co₃O₄ Nanoparticles Anchored on Nitrogen-Doped Reduced Graphene Oxide as a Multifunctional Catalyst for H₂O₂ Reduction, Oxygen Reduction and Evolution Reaction. *Sci. Rep.* **2017**, *7*, 43638. [[CrossRef](#)] [[PubMed](#)]
9. Singh, K.P.; Bae, E.J.; Yu, J.-S. Fe-P: A New Class of Electroactive Catalyst for Oxygen Reduction Reaction. *J. Am. Chem. Soc.* **2015**, *137*, 3165–3168. [[CrossRef](#)] [[PubMed](#)]
10. Sa, Y.J.; Seo, D.-J.; Woo, J.; Lim, J.T.; Cheon, J.Y.; Yang, S.Y.; Lee, J.M.; Kang, D.; Shin, T.J.; Shin, H.S. A General Approach to Preferential Formation of Active Fe-N X Sites in Fe-N/C Electrocatalysts for Efficient Oxygen Reduction Reaction. *J. Am. Chem. Soc.* **2016**, *138*, 15046–15056. [[CrossRef](#)] [[PubMed](#)]
11. Ma, M.; You, S.; Wang, W.; Liu, G.; Qi, D.; Chen, X.; Qu, J.; Ren, N. Biomass-Derived Porous Fe₃C/Tungsten Carbide/Graphitic Carbon Nanocomposite for Efficient Electrocatalysis of Oxygen Reduction. *ACS Appl. Mater. Interfaces* **2016**, *8*, 32307–32316. [[CrossRef](#)] [[PubMed](#)]
12. Park, M.J.; Lee, J.H.; Hembram, K.; Lee, K.-R.; Han, S.S.; Yoon, C.W.; Nam, S.-W.; Kim, J.Y. Oxygen Reduction Electrocatalysts Based on Coupled Iron Nitride Nanoparticles with Nitrogen-Doped Carbon. *Catalysts* **2016**, *6*, 86. [[CrossRef](#)]
13. Zhang, T.; He, C.; Li, L.; Lin, Y. Preparation of Nitrogen-Doped Carbon Nanoblocks with High Electrocatalytic Activity for Oxygen Reduction Reaction in Alkaline Solution. *Chin. J. Catal.* **2016**, *37*, 1275–1282. [[CrossRef](#)]
14. Wang, Y.-J.; Wilkinson, D.P.; Zhang, J. Noncarbon Support Materials for Polymer Electrolyte Membrane Fuel Cell Electrocatalysts. *Chem. Rev.* **2011**, *111*, 7625–7651. [[CrossRef](#)] [[PubMed](#)]
15. Xia, W.; Mahmood, A.; Liang, Z.; Zou, R.; Guo, S. Earth-Abundant Nanomaterials for Oxygen Reduction. *Angew. Chem. Int. Ed.* **2016**, *55*, 2650–2676. [[CrossRef](#)] [[PubMed](#)]

16. Tachibana, N.; Ikeda, S.; Yukawa, Y.; Kawaguchi, M. Highly Porous Nitrogen-Doped Carbon Nanoparticles Synthesized Via Simple Thermal Treatment and Their Electrocatalytic Activity for Oxygen Reduction Reaction. *Carbon* **2017**, *115*, 515–525. [[CrossRef](#)]
17. Xue, H.; Wang, T.; Gong, H.; Guo, H.; Fan, X.; Song, L.; Xia, W.; Feng, Y.; He, J. Co₃O₄ Nanoparticle-Decorated N-Doped Mesoporous Carbon Nanofibers as an Efficient Catalyst for Oxygen Reduction Reaction. *Catalysts* **2017**, *7*, 189. [[CrossRef](#)]
18. He, C.; Li, L.; Zhang, T.; Sun, F.; Wang, C.; Lin, Y. Nitrogen-Doped Amorphous Carbon with Effective Electrocatalytic Activity toward Oxygen Reduction Reaction. *Mater. Res. Bull.* **2016**, *84*, 118–123. [[CrossRef](#)]
19. Chung, M.W.; Choi, C.H.; Lee, S.Y.; Woo, S.I. Dimensionality-Dependent Oxygen Reduction Activity on Doped Graphene: Is Graphene a Promising Substrate for Electrocatalysis? *Nano Energy* **2015**, *11*, 526–532. [[CrossRef](#)]
20. Zhu, H.; Sun, Z.; Chen, M.; Cao, H.; Li, K.; Cai, Y.; Wang, F. Highly Porous Composite Based on Tungsten Carbide and N-Doped Carbon Aerogels for Electrocatalyzing Oxygen Reduction Reaction in Acidic and Alkaline Media. *Electrochim. Acta.* **2017**, *236*, 154–160. [[CrossRef](#)]
21. Rivera, L.M.; Fajardo, S.; Arévalo, M.D.C.; García, G.; Pastor, E. S- and N-Doped Graphene Nanomaterials for the Oxygen Reduction Reaction. *Catalysts* **2017**, *7*, 278. [[CrossRef](#)]
22. Zheng, J.; Zhou, W.; Liu, T.; Liu, S.; Wang, C.; Guo, L. Homologous NiO//Ni₂P Nanoarrays Grown on Nickel Foams: A Well Matched Electrode Pair with High Stability in Overall Water Splitting. *Nanoscale* **2017**, *9*, 4409–4418. [[CrossRef](#)] [[PubMed](#)]
23. Wu, Z.-S.; Yang, S.; Sun, Y.; Parvez, K.; Feng, X.; Müllen, K. 3D Nitrogen-Doped Graphene Aerogel-Supported Fe₃O₄ Nanoparticles as Efficient Electrocatalysts for the Oxygen Reduction Reaction. *J. Am. Chem. Soc.* **2012**, *134*, 9082–9085. [[CrossRef](#)] [[PubMed](#)]
24. Zhou, W.; Ge, L.; Chen, Z.-G.; Liang, F.; Xu, H.-Y.; Motuzas, J.; Julbe, A.; Zhu, Z. Amorphous Iron Oxide Decorated 3D Heterostructured Electrode for Highly Efficient Oxygen Reduction. *Chem. Mater.* **2011**, *23*, 4193–4198. [[CrossRef](#)]
25. Li, M.; Xiong, Y.; Liu, X.; Han, C.; Zhang, Y.; Bo, X.; Guo, L. Iron and Nitrogen Co-Doped Carbon Nanotubes@Hollow Carbon Fibers Derived from Plant Biomass as Efficient Catalysts for Oxygen Reduction Reaction. *J. Mater. Chem. A* **2015**, *3*, 9658–9667. [[CrossRef](#)]
26. Zhou, K.; Zhou, W.; Liu, X.; Wang, Y.; Wan, J.; Chen, S. Nitrogen Self-Doped Porous Carbon from Surplus Sludge as Metal-Free Electrocatalysts for Oxygen Reduction Reactions. *ACS Appl. Mater. Interfaces* **2014**, *6*, 14911–14918. [[CrossRef](#)] [[PubMed](#)]
27. Li, J.-C.; Hou, P.-X.; Zhao, S.-Y.; Liu, C.; Tang, D.-M.; Cheng, M.; Zhang, F.; Cheng, H.-M. A 3D Bi-Functional Porous N-Doped Carbon Microtube Sponge Electrocatalyst for Oxygen Reduction and Oxygen Evolution Reactions. *Energy Environ. Sci.* **2016**, *9*, 3079–3084. [[CrossRef](#)]
28. Raj, C.R.; Samanta, A.; Noh, S.H.; Mondal, S.; Okajima, T.; Ohsaka, T. Emerging New Generation Electrocatalysts for the Oxygen Reduction Reaction. *J. Mater. Chem. A* **2016**, *4*, 11156–11178. [[CrossRef](#)]
29. Zang, Y.; Zhang, H.; Zhang, X.; Liu, R.; Liu, S.; Wang, G.; Zhang, Y.; Zhao, H. Fe/Fe₂O₃ Nanoparticles Anchored on Fe-N-Doped Carbon Nanosheets as Bifunctional Oxygen Electrocatalysts for Rechargeable Zinc-Air Batteries. *Nano Res.* **2016**, *9*, 2123–2137. [[CrossRef](#)]
30. Vezzù, K.; Delpeuch, A.B.; Negro, E.; Polizzi, S.; Nawn, G.; Bertasi, F.; Pagot, G.; Artyushkova, K.; Atanassov, P.; Di Noto, V. Fe-Carbon Nitride “Core-Shell” Electrocatalysts for the Oxygen Reduction Reaction. *Electrochim. Acta.* **2016**, *222*, 1778–1791. [[CrossRef](#)]
31. Wu, H.; Geng, J.; Ge, H.; Guo, Z.; Wang, Y.; Zheng, G. Egg-Derived Mesoporous Carbon Microspheres as Bifunctional Oxygen Evolution and Oxygen Reduction Electrocatalysts. *Adv. Energy Mater.* **2016**, *6*, 1600794. [[CrossRef](#)]
32. Hu, B.; Wang, K.; Wu, L.; Yu, S.H.; Antonietti, M.; Titirici, M.M. Engineering Carbon Materials from the Hydrothermal Carbonization Process of Biomass. *Adv. Mater.* **2010**, *22*, 813–828. [[CrossRef](#)] [[PubMed](#)]
33. Ma, N.; Jia, Y.A.; Yang, X.; She, X.; Zhang, L.; Peng, Z.; Yao, X.; Yang, D. Seaweed Biomass Derived (Ni, Co)/Cnt Nanoaerogels: Efficient Bifunctional Electrocatalysts for Oxygen Evolution and Reduction Reactions. *J. Mater. Chem. A* **2016**, *4*, 6376–6384. [[CrossRef](#)]
34. Li, Q.; Cao, R.; Cho, J.; Wu, G. Nanocarbon Electrocatalysts for Oxygen Reduction in Alkaline Media for Advanced Energy Conversion and Storage. *Adv. Energy Mater.* **2014**, *4*, 1301415. [[CrossRef](#)]

35. Choi, C.H.; Chung, M.W.; Kwon, H.C.; Chung, J.H.; Woo, S.I. Nitrogen-Doped Graphene/Carbon Nanotube Self-Assembly for Efficient Oxygen Reduction Reaction in Acid Media. *Appl. Catal. B* **2014**, *144*, 760–766. [[CrossRef](#)]
36. Yang, G.; Choi, W.; Pu, X.; Yu, C. Scalable Synthesis of Bi-Functional High-Performance Carbon Nanotube Sponge Catalysts and Electrodes with Optimum C-N-Fe Coordination for Oxygen Reduction Reaction. *Energy Environ. Sci.* **2015**, *8*, 1799–1807. [[CrossRef](#)]
37. Bennett, J.A.; Wilson, K.; Lee, A.F. Catalytic Applications of Waste Derived Materials. *J. Mater. Chem. A* **2016**, *4*, 3617–3637. [[CrossRef](#)]
38. González-García, E.; Martín Martín, G. Biomass Yield and Nutrient Content of a Tropical Mulberry Forage Bank: Effects of Season, Harvest Frequency and Fertilization Rate. *Grass Forage Sci.* **2017**, *72*, 248–260. [[CrossRef](#)]
39. Lee, S.; Kwak, D.-H.; Han, S.-B.; Lee, Y.-W.; Lee, J.-Y.; Choi, I.-A.; Park, H.-S.; Park, J.-Y.; Park, K.-W. Bimodal Porous Iron/Nitrogen-Doped Highly Crystalline Carbon Nanostructure as a Cathode Catalyst for the Oxygen Reduction Reaction in an Acid Medium. *ACS Catal.* **2016**, *6*, 5095–5102. [[CrossRef](#)]
40. Zhang, Y.; Huang, L.-B.; Jiang, W.-J.; Zhang, X.; Chen, Y.-Y.; Wei, Z.; Wan, L.-J.; Hu, J.-S. Sodium Chloride-Assisted Green Synthesis of a 3D Fe-N-C Hybrid as a Highly Active Electrocatalyst for the Oxygen Reduction Reaction. *J. Mater. Chem. A* **2016**, *4*, 7781–7787. [[CrossRef](#)]
41. Zhou, D.; Yang, L.; Yu, L.; Kong, J.; Yao, X.; Liu, W.; Xu, Z.; Lu, X. Fe/N/C Hollow Nanospheres by Fe (iii)-Dopamine Complexation-Assisted One-Pot Doping as Nonprecious-Metal Electrocatalysts for Oxygen Reduction. *Nanoscale* **2015**, *7*, 1501–1509. [[CrossRef](#)] [[PubMed](#)]
42. Pedrazzetti, L.; Soltani, P.; Mezzi, A.; Kaciulis, S.; Nobili, L.; Tommasini, M.M.S.; Magagnin, L. Galvanic Displaced Nickel-Silicon and Copper-Silicon Interfaces: A Dft Investigation. *ECS Trans.* **2017**, *75*, 7–13. [[CrossRef](#)]
43. Deng, C.; Ding, F.; Li, X.; Guo, Y.; Ni, W.; Yan, H.; Sun, K.; Yan, Y.-M. Templated-Preparation of a Three-Dimensional Molybdenum Phosphide Sponge as a High Performance Electrode for Hydrogen Evolution. *J. Mater. Chem. A* **2016**, *4*, 59–66. [[CrossRef](#)]
44. Zhang, Y.-X.; Guo, X.; Zhai, X.; Yan, Y.-M.; Sun, K.-N. Diethylenetriamine (Deta)—Assisted Anchoring of Co₃O₄ Nanorods on Carbon Nanotubes as Efficient Electrocatalysts for the Oxygen Evolution Reaction. *J. Mater. Chem. A* **2015**, *3*, 1761–1768. [[CrossRef](#)]
45. Yang, L.; Su, Y.; Li, W.; Kan, X. Fe/N/C Electrocatalysts for Oxygen Reduction Reaction in Pem Fuel Cells Using Nitrogen-Rich Ligand as Precursor. *J. Phys. Chem. C* **2015**, *119*, 11311–11319. [[CrossRef](#)]
46. Guo, Z.; Xiao, Z.; Ren, G.; Xiao, G.; Zhu, Y.; Dai, L.; Jiang, L. Natural Tea-Leaf-Derived, Ternary-Doped 3D Porous Carbon as a High-Performance Electrocatalyst for the Oxygen Reduction Reaction. *Nano Res.* **2016**, *9*, 1244–1255. [[CrossRef](#)]
47. Wang, M.-Q.; Yang, W.-H.; Wang, H.-H.; Chen, C.; Zhou, Z.-Y.; Sun, S.-G. Pyrolyzed Fe-N-C Composite as an Efficient Non-Precious Metal Catalyst for Oxygen Reduction Reaction in Acidic Medium. *ACS Catal.* **2014**, *4*, 3928–3936. [[CrossRef](#)]
48. Yu, L.; Shen, Y.; Huang, Y. Fe-N-C Catalyst Modified Graphene Sponge as a Cathode Material for Lithium-Oxygen Battery. *J. Alloys Compd.* **2014**, *595*, 185–191. [[CrossRef](#)]
49. Videla, A.H.A.M.; Ban, S.; Specchia, S.; Zhang, L.; Zhang, J. Non-Noble Fe-N X Electrocatalysts Supported on the Reduced Graphene Oxide for Oxygen Reduction Reaction. *Carbon* **2014**, *76*, 386–400. [[CrossRef](#)]
50. Huang, L.; Zhao, C.; Yao, Y.; You, Y.; Wang, Z.; Wu, C.; Sun, Y.; Tian, J.; Liu, J.; Zou, Z. Fe/N/C Catalyst with High Activity for Oxygen Reduction Reaction Derived from Surfactant Modified Porous Carbon-Supported Melamine-Formaldehyde Resin. *Int. J. Hydrog. Energy* **2016**, *41*, 11090–11098. [[CrossRef](#)]
51. Parvez, K.; Yang, S.; Hernandez, Y.; Winter, A.; Turchanin, A.; Feng, X.; Müllen, K. Nitrogen-Doped Graphene and Its Iron-Based Composite as Efficient Electrocatalysts for Oxygen Reduction Reaction. *ACS Nano* **2012**, *6*, 9541–9550. [[CrossRef](#)] [[PubMed](#)]
52. Zhang, Y.; Ding, F.; Deng, C.; Zhen, S.; Li, X.; Xue, Y.; Yan, Y.-M.; Sun, K. Crystal Plane-Dependent Electrocatalytic Activity of Co₃O₄ toward Oxygen Evolution Reaction. *Catal. Commun.* **2015**, *67*, 78–82. [[CrossRef](#)]
53. Wan, W.; Wang, Q.; Zhang, L.; Liang, H.; Chen, P.; Yu, S.H. N-, P- and Fe- Tridoped Nanoporous Carbon Derived from Plant Biomass: An Excellent Oxygen Reduction Electrocatalyst for Zinc-Air Battery. *J. Mater. Chem. A* **2016**, *4*, 8602–8609. [[CrossRef](#)]

54. Razmjooei, F.; Singh, K.P.; Yu, J.S. Superior Pore Network Retention of Carbon Derived from Naturally Dried Ginkgo Leaves and Its Enhanced Oxygen Reduction Performance. *Catal. Today* **2015**, *260*, 148–157. [[CrossRef](#)]
55. Gao, S.; Fan, H.; Zhang, S. Nitrogen-Enriched Carbon from Bamboo Fungus with Superior Oxygen Reduction Reaction Activity. *J. Mater. Chem. A* **2014**, *2*, 18263–18270. [[CrossRef](#)]
56. Guo, C.; Liao, W.; Li, Z.; Sun, L.; Chen, C. Easy Conversion of Protein-Rich Enoki Mushroom Biomass to a Nitrogen-Doped Carbon Nanomaterial as a Promising Metal-Free Catalyst for Oxygen Reduction Reaction. *Nanoscale* **2015**, *7*, 15990. [[CrossRef](#)] [[PubMed](#)]



© 2018 by the authors. Licensee MDPI, Basel, Switzerland. This article is an open access article distributed under the terms and conditions of the Creative Commons Attribution (CC BY) license (<http://creativecommons.org/licenses/by/4.0/>).